A Turbulence-resolving Numerical Model for Fine Sediment Transport in the Bottom Boundary Layer — FineSed3D (Version 1.0)

BY

ZHEN CHENG[1], XIAO YU[1], CELALETTIN EMRE OZDEMIR[2], TIAN-JIAN HSU[1] AND SIVARAMAKRISHNAN BALACHANDAR[3]

[1]CENTER FOR APPLIED COASTAL RESEARCH, UNIVERSITY OF DELAWARE, NEWARK, DE 19716
[2]CIVIL AND ENVIRONMENTAL ENGINEERING, LOUISIANA STATE UNIVERSITY, BATON ROUGE, LA 70803
[3]MECHANICAL AND AEROSPACE ENGINEERING, UNIVERSITY OF FLORIDA, GAINESVILLE, FL 32611

RESEARCH REPORT NO. CACR-15-01
JANUARY 2015

CENTER FOR APPLIED COASTAL RESEARCH

Ocean Engineering Laboratory
University of Delaware
Newark, Delaware 19716, USA

Acknowledgements

This work is supported by National Science Foundation (OCE-1130217) and Office of Naval Research (N00014-14-1-0586) to the University of Delaware and National Science Foundation (OCE-1131016) to the University of Florida. Simulations presented in this paper are carried out on Chimera at the University of Delaware with funding supported by the National Science Foundation (CNS-0958512) and the Extreme Science and Engineering Discovery Environment, which is supported by National Science Foundation Grant No. TG-OCE100015.

Abstract

A turbulence-resolving numerical model for fine sediment transport in the bottom boundary layer is developed. A simplified Eulerian two-phase flow formulation for the fine sediment transport is adopted. By applying the equilibrium Eulerian approximation, the particle phase velocity is expressed as a vectorial sum of fluid velocity, sediment settling velocity and Stokes number dependent inertia terms. The Boussinesq approximation is applied to simplify the governing equation for the fluid phase. This model utilizes a high accuracy hybrid compact finite difference scheme in the wall-normal direction, and uses the pseudo-spectral scheme in the streamwise and spanwise directions. The model allows a prescribed sediment availability as well as an erosional/depositional bottom boundary condition for sediment concentration. As an example, several numerical simulations are presented to study how the bottom resuspension/deposition mechanisms, specifically the critical shear stress of erosion and the settling velocity, can determine the sediment availability and the resulting transport modes. Meanwhile, the model also has the capability to include the particle inertia effect and hindered settling effect for the particle velocity. This report is written as the documentation of this open-source numerical model **FineSed3D** and it includes the mathematical formulations, numerical methodology, brief model results, installation procedures and model input/output.

Contents

List of Figures

List of Tables

1 Introduction

In many estuaries and continental shelves, the delivery and dispersal of fine sediment play a critical role in determining coastal geomorphology (*Friedrichs and Wright*, 2004), carbon cycle (*Goldsmith et al.*, 2008) and ecosystem processes. In addition to currents, waves are known to play a critical role in delivering these fine sediments (e.g., *Wiberg et al.*, 1994), especially in the cross-shelf direction via sediment flux gradients (*Harris and Wiberg*, 1997, 2002) and sediment-driven gravity flows (*Traykovski et al.*, 2000; *Ogston et al.*, 2000; *Hale et al.*, 2014).

On this subject, several previous turbulence-resolving numerical studies also suggested that sediment-induced density stratification plays an important role (e.g., *Ozdemir et al.*, 2010, 2011; *Yu et al.*, 2014; *Cheng et al.*, 2015a). Simulation results revealed that at a given Stokes Reynolds number, the prescribed sediment load and settling velocity determine the degree of sediment-induced density stratification and lead to four distinct flow regimes (*Ozdemir et al.*, 2010, 2011): Regime I is of very dilute flow (sediment concentration is much smaller than $\sim$ 1 g/L), sediments are well-mixed and the carrier fluid turbulence remains intact within the boundary layer. Regime II occurs when the near-bed sediment concentration is in the range of $O\big(1 \sim 10\big)$ g/L, and lutocline, i.e., a sharp negative concentration gradient, is formed. Above the lutocline, the flow becomes quasi-laminar but it remains turbulent beneath. Regime III takes place when the near bed sediment concentration approaches several tens of g/L, carrier fluid turbulence is significantly attenuated, and flow becomes nearly laminar. However, due to shear instability sediment burst events occur during flow reversal. Regime IV is observed at sediment concentration of $O\big(100\big)$ g/L or greater, in which a completely laminarized flow throughout the wave cycle is observed. The existence of these regimes and the transition from one regime to the other have critical implications to our capability in assessing the state of the muddy seabed and to further understand various applications related to the fine sediment transport.

Flux convergence (e.g., *Wright and Friedrichs*, 2006) and bottom resuspension determine the source of fine sediments in the water column (e.g., *Wheatcroft and Borgeld*, 2000; *Fan et al.*, 2004; *Bever et al.*, 2011). Hence, characterizing the resuspension of fine sediment in the wave bottom boundary layer (WBBL) is an important segment of sediment source to sink. There are many studies about the fine sediment resuspension and deposition for tidal bottom boundary layers (e.g., *Winterwerp*, 2006; *Byun and Wang*, 2005) and WBBL (e.g., *Hsu et al.*, 2009). However, these numerical studies are based on Reynolds-averaged models. Due to underlying assumptions adopted in the turbulence closure (for example, the assumption of fully turbulent flow) and the transitional nature of the WBBL (e.g., *Ozdemir et al.*, 2014), Reynolds-averaged models may not be sufficiently accurate to investigate the effect of turbulence modulation due to sediment, especially when it is

related to the onset of laminarization.

In most of the models for fine sediment transport, the particle velocity can be calculated by the equilibrium Eulerian approximation (*Balachandar and Eaton*, 2010), that is, a vectorial sum of the local fluid velocity, the settling velocity and additional particle inertia terms associated with the Stokes number. This approximation is only appropriate for particles of Stokes number much smaller than unity. From the theoretical perspective (*Balachandar and Eaton*, 2010), the particle inertia effect is another mechanism to deviate the particle velocity from the fluid velocity, especially in turbulent flow with high acceleration (*Cantero et al.*, 2008). However, these additional terms are also ignored in the aforementioned turbulence-resolving studies (e.g., *Ozdemir et al.*, 2010; *Yu et al.*, 2013; *Cheng et al.*, 2015a). There is a need to quantify the effect of neglecting the particle inertia on fine sediment transport for typical wave conditions encountered in the continental shelves.

Meanwhile, the settling velocities are often assumed to be constant for simplicity in the studies of *Ozdemir et al.* (2010) and *Yu et al.* (2014). However, due to interactions among descending particles, upward flow motions are generated and hence the collective settling velocity of particles is reduced from the single particle settling velocity. This is the well-known hindered settling effect (e.g., *Winterwerp and Van Kesteren*, 2004; *Fredsoe and Deigaard*, 1992). For non-cohesive sediments, hindered settling is a relatively well-constrained process (*Richardson and Zaki*, 1954; *Jimenez and Madsen*, 2003). For example, the reference concentration, often introduced in the hindered settling parameterization, is generally agreed to be the random-close-packing concentration of sediment (around 0.6 in term of volumetric concentration). For fine sediments that often become cohesive in the coastal waters, the hindered settling plays a critical role in the slow deposition and consolidation processes. However, the parameterization of hindered settling for cohesive sediment is poorly constrained due to uncertainties in flocculation. When flocs are considered, the 'gelling concentration' is typically introduced to replace the reference concentration in the hindered settling parameterization (*Dankers and Winterwerp*, 2007), and it is defined as the concentration at which floc aggregates form concentrated aggregate networks (*Winterwerp and Van Kesteren*, 2004). However, the gelling concentration has a wide range of values due to variabilities in floc structures. For more organic and porous flocs with low fractal dimensions, the gelling concentration can be as low as $\sim$100 g/L.

In summary, a turbulence-resolving model with the capability to study sediment transport dynamics on an erodible bed is needed. The effects of particle inertia and hindered settling need to be evaluated for a comprehensive understanding of the fine sediment transport in natural environments. The objective of this report is to present such model. The model formulations are discussed in Section 2. In section 3, numerical methodologies are discussed. In section 4, results of numerical experiments are presented to illustrate

the effect of sediment erodibility and settling velocity on controlling the resulting transport characteristics. The sensitivities of the particle inertial effect and hindered settling effect for typical energetic wave conditions in the inner-shelves are also evaluated. Conclusions and future works are presented in Section 5. Finally, the model installation and input/output are documented in the Appendix.

2 Model Formulations

2.1 Governing Equations

Although the present numerical model can be used to study fine sediment in the steady flow boundary layer (see more details in *Yu et al.* (2013)), for conciseness, we will only discuss the capability of studying fine sediment transport in the oscillatory boundary layer. We consider a typical wave condition with a free-stream velocity magnitude of $\widetilde{U}_0$ and a wave period of $\widetilde{T}$, and the fine sediment is of grain size $\tilde{d}$ with a specific gravity $s = \rho_s/\rho_f$, where ρ_s is the sediment density, and ρ_f is the carrier fluid density. A simplified Eulerian two-phase flow formulation for the fine sediment transport is adopted (*Ferry and Balachandar*, 2001). For fine sediment transport, the equilibrium Eulerian approximation (*Ferry et al.*, 2003; *Balachandar and Eaton*, 2010) can be applied (*Ozdemir et al.*, 2010; *Yu et al.*, 2014; *Cheng et al.*, 2015a,b). Thus, the particle velocity $\tilde{u}_i^s$ can be simplified to be an algebraical sum of the fluid velocity $\tilde{u}_i$, the settling velocity $\widetilde{W}_{s0}$ and an expansion in terms of the particle response time $\tilde{t}_p$:

$$\tilde{u}_i^s = \tilde{u}_i - \tilde{W}_{s0}\delta_{i3} - \tilde{t}_p(1 - \frac{1}{s})\frac{D\tilde{u}_i}{D\tilde{t}} + H.O.T., \tag{1}$$

where $i = 1, 2, 3$ represents streamwise (x), spanwise (y) and vertical (z) directions, respectively. The settling velocity $\tilde{W}_{s0}$ is calculated according to the Stokes' law:

$$\tilde{W}_{s0} = \frac{(s-1)g\tilde{d}^2}{18\nu}, \tag{2}$$

where ν is the kinematic viscosity of fluid phase, and $g = 9.81$ m/s^2 is the gravitational acceleration. $\tilde{t}_p$ is the particle response time, which is defined as:

$$\tilde{t}_p = \frac{s\tilde{d}^2}{18\nu}, \tag{3}$$

The equilibrium Eulerian approximation is justified for fine particulate flows where the particle response time is sufficiently smaller than the characteristic fluid time scale (*Ferry et al.*, 2003). In this paper, except for physical constants such as ρ_f, ρ_s, ν, g and the sediment diffusivity κ, variables without overhead '$\sim$' are non-dimensional variables.

For the suspended sediment transport in typical continental shelves, the volumetric concentration of sediment is usually not significant (< 0.05) (*Traykovski et al.*, 2007). Therefore, the density variation is sufficiently small such that the Boussinesq approximation can be adopted to simplify the governing equations. By substituting Eq. (1) into the Eulerian two-phase equations for the fluid phase (*Cantero et al.*, 2008), and applying the

Boussinesq approximation, the resulting continuity and momentum equations for the fluid flow read as:

$$\frac{\partial \tilde{u}_i}{\partial \tilde{x}_i} = 0, \tag{4}$$

$$\frac{\partial \tilde{u}_i}{\partial \tilde{t}} + \tilde{u}_j \frac{\partial \tilde{u}_i}{\partial \tilde{x}_j} = -\frac{1}{\rho_f}\frac{\partial \tilde{p}}{\partial \tilde{x}_i} - \tilde{U}_0 \tilde{\omega} \sin\left(\tilde{\omega}\tilde{t}\right)\delta_{i1} + \nu \frac{\partial^2 \tilde{u}_i}{\partial \tilde{x}_j \partial \tilde{x}_j} - (s-1) g \phi \delta_{i3}, \tag{5}$$

where the fluid dynamic pressure is represented by $\tilde{p}$, and ϕ is the volumetric concentration of sediment, which is dimensionless. The second term on the right-hand-side of equation (5) is the streamwise pressure gradient that drives the prescribed wave motion, where $\tilde{\omega}$ is the wave angular frequency, $\tilde{\omega} = 2\pi/\widetilde{T}$. The last term on the right-hand-side of equation (5) represents the coupling between the sediment phase and the carrier fluid via the sediment-induced density stratification.

The governing equation of sediment concentration is written as:

$$\frac{\partial \phi}{\partial \tilde{t}} + \frac{\partial \tilde{u}_i^s \phi}{\partial \tilde{x}_i} = \kappa \frac{\partial^2 \phi}{\partial \tilde{x}_i \partial \tilde{x}_i}. \tag{6}$$

where the particle velocity $\tilde{u}_i^s$ is calculated by the equilibrium Eulerian approximation (Eq. (1)).

To generalize the simulation results, flow variables are nondimensionalized and a set of dimensionless equations are solved in the numerical model. The free-stream velocity amplitude $\widetilde{U}_0$ is chosen as the characteristic velocity scale, and the Stokes boundary layer thickness $\widetilde{\Delta}$ is selected to be the characteristic length scale of the flow:

$$\tilde{\Delta} = \sqrt{\frac{2\nu}{\tilde{\omega}}}. \tag{7}$$

Consequently, the flow characteristic time scale is calculated as $\tilde{t}_l = \widetilde{\Delta}/\widetilde{U}_0$, and the non-dimensional flow variables can be defined as:

$$x_i = \frac{\tilde{x}_i}{\widetilde{\Delta}}, t = \frac{\tilde{t}}{\tilde{t}_l}, u_i = \frac{\tilde{u}_i}{\widetilde{U}_0}, u_i^s = \frac{\tilde{u}_i^s}{\widetilde{U}_0}, W_{s0} = \frac{\tilde{W}_{s0}}{\widetilde{U}_0}, p = \frac{\tilde{p}}{\rho_f \widetilde{U}_0^2}. \tag{8}$$

Normalized by the above characteristic flow scales, the non-dimensional particle velocity u_i^s becomes:

$$u_i^s = u_i - W_{s0}\delta_{i3} - St(1 - \frac{1}{s})\frac{Du_i}{Dt} + \mathcal{O}(St). \tag{9}$$

where the particle Stokes number $St = \tilde{t}_p/\tilde{t}_l$ is introduced to quantify the particle inertia relative to the flow inertia.

The resulting non-dimensional continuity and momentum equations for fluid flow are written as:

$$\frac{\partial u_i}{\partial x_i} = 0, \tag{10}$$

$$\frac{\partial u_i}{\partial t} + u_j \frac{\partial u_i}{\partial x_j} = -\frac{\partial p}{\partial x_i} - \frac{2}{Re_\Delta} \sin\left(\frac{2t}{Re_\Delta}\right)\delta_{i1} + \frac{1}{Re_\Delta}\frac{\partial^2 u_i}{\partial x_j \partial x_j} - \frac{1}{Fr^2}\phi\delta_{i3}, \tag{11}$$

where $Re_\Delta = \tilde{U}_0\tilde{\Delta}/\nu$ is the Stokes Reynolds number, which is used to quantify the wave intensity. In the previous studies of *Ozdemir et al.* (2010, 2011), the total amount of sediment in the domain is prescribed and maintained as constant in each simulation (a no-flux boundary condition for sediment at both the bottom and top boundaries are enforced) and hence the last term in equation (11) is represented by a bulk Richardson number (*Ozdemir et al.*, 2010, 2011). Recently, an erosional/depositional bottom boundary is implemented in the model and the total amount of sediment in the domain is part of the solution of the model (*Cheng et al.*, 2015a). Therefore, the particle Froude number $Fr = \tilde{U}_0/\sqrt{(s-1)g\tilde{\Delta}}$ is introduced instead.

The non-dimensional transport equation for sediment concentration is written as:

$$\frac{\partial \phi}{\partial t} + \frac{\partial u_i^s \phi}{\partial x_i} = \frac{1}{Re_\Delta Sc}\frac{\partial^2 \phi}{\partial x_i \partial x_i}, \tag{12}$$

where Sc is the Schmidt number, $Sc = \nu/\kappa$. The right-hand-side of equation (12) accounts for the sub-grid scale particle motion.

2.2 Boundary Conditions

The bottom boundary layer is idealized to be statistically homogeneous in streamwise (x) and spanwise (y) directions (see Fig. 1). Periodic boundary conditions are used along streamwise and spanwise boundaries for fluid phase velocities and the sediment concentration. Two walls are located at the top and bottom boundaries and no-slip and no-penetration wall boundary conditions are implemented for the fluid velocity. For the sediment concentration, the no-flux boundary condition is applied at the top boundary:

$$w^s\phi - \frac{1}{Re_\Delta Sc}\frac{\partial \phi}{\partial z}\Big|_{z=L_z} = 0, \tag{13}$$

where $z = L_z$ is located at the top of the domain, and w^s is the vertical component of the sediment velocity.

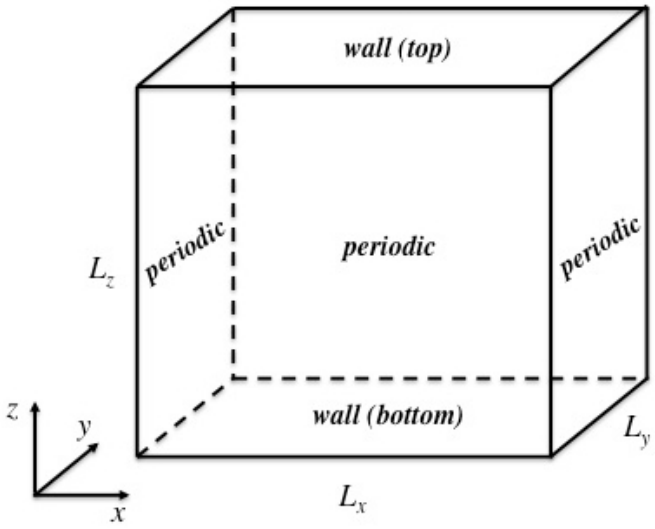

Fig. 1: Illustration of computation domain and coordinate system.

At the bottom boundary, an erodible/depositional boundary condition is implemented for sediment concentration to allow resuspension/deposition at the bottom:

$$w^s\phi - \frac{1}{Re_\Delta Sc}\frac{\partial\phi}{\partial z}\Big|_{z=0} = E - D, \tag{14}$$

where E and D are the non-dimensional erosional and depositional fluxes at the bottom, respectively, and both E and D are normalized by the free-stream velocity magnitude $\tilde{U}_0$. When the sediment availability is kept constant in the domain, no-flux boundary condition, i.e., $E = D$ is enforced at the bottom boundary (*Ozdemir et al.*, 2010, 2011; *Yu et al.*, 2014). Another option is to utilize the empirical bottom erosion and deposition models for fine sediment and the sediment availability in the domain is determined by the interplay of the sediment erosional flux and the depositional flux at the bottom boundary. Since many empirical parameters involved in erosional/depositional formulas are measured or presented in dimensional forms (e.g., *Hill et al.*, 2000; *Sanford and Maa*, 2001), the dimensional forms of the depositional flux and the erosional flux are discussed here. The depositional flux is specified following the continuous erosion-deposition formulation (*Sanford and Maa*, 2001; *Winterwerp*, 2007):

$$\tilde{D} = -\tilde{w}_s\phi\Big|_{\tilde{z}=0}. \tag{15}$$

The erosion rate $\tilde{E}$ is calculated by the Partheniades-Ariathurai type formulation (e.g.,

Sanford and Maa, 2001), and it is presented here in the non-dimensional form:

$$\tilde{E} = \begin{cases} \tilde{m}_e\left(\frac{|\tilde{\tau}_b|}{\tilde{\tau}_c} - 1\right), & |\tilde{\tau}_b| \geq \tilde{\tau}_c \\ 0, & |\tilde{\tau}_b| < \tilde{\tau}_c \end{cases}, \tag{16}$$

where $\tilde{m}_e$ is the dimensional empirical coefficient of erosion rate, $|\widetilde{\tau}_b|$ is the magnitude of the bottom shear stress, and it is calculated as:

$$|\widetilde{\tau}_b| = \rho_f \nu \left|\frac{\partial \widetilde{u}}{\partial \widetilde{z}}\right|_{\widetilde{z}=0}, \tag{17}$$

and the critical shear stress of erosion is represented by $\tilde{\tau}_c$. For fine sediments, both $\tilde{m}_e$ and $\tilde{\tau}_c$ depend on the degree of consolidation, and need to be determined from erosion tests.

3 Numerical Method

A recently developed turbulence-resolving hybrid spectral-compact finite difference scheme for the fine sediment transport in bottom boundary layer (*Yu et al.*, 2013) is utilized. In this numerical model, the computation domain (see Fig. 1) is assumed to be statistically homogeneous in the streamwise and spanwise directions. Fourier expansions are adopted in both streamwise and spanwise directions, which enforce the periodic boundary conditions in these directions, and uniform grids in both streamwise and spanwise directions. More details on the pseudo-spectral scheme of the present model can be found in *Cortese and Balachandar* (1995). In the vertical (wall-normal) direction, Chebyshev collocation points are used, where more grid points are clustered at both the top and the bottom boundaries, and a sixth-order centered compact finite difference scheme is implemented. With this extension, more complicated (nonlinear) boundary conditions, such as erodible/depositional boundary condition for sediments, can be implemented while maintaining spectral-like accuracy. More details on the compact finite difference scheme of the present model can be found in *Yu et al.* (2013, 2014). Eq. (10) and (11) are solved with a standard projection method (*Chorin*, 1968). For diffusion terms, the Crank-Nicolson scheme is used. Nonlinear advection terms are calculated by the Arakawa method (*Arakawa and Lamb*, 1981) with the $2/3$ de-aliasing law, and integrated by a third-order low-storage Runge-Kutta scheme. A direct solver (*Yu et al.*, 2013) is used to solve the pressure Poisson equation. For the equation of sediment concentration, same numerical methods are used where applicable.

Notice that the effective settling velocity may vary with x and y if hindered settling or particle inertia is considered. To satisfy the mass conservation at the top boundary, the no-flux boundary condition (Eq. (13)) should be satisfied. In the present numerical schemes, Fourier expansions are adopted in both streamwise and spanwise directions. If we transfer Eq. (13) into Fourier space, convolution terms will arise from the nonlinear multiplication term (first term on left-hand-side of Eq. (13)), which is difficult to handle. To resolve this problem, the sediment velocity at the top boundary is decomposed into x-y plane-averaged component $\langle w^s \rangle$ and the fluctuation component $w^{s\prime}$:

$$w^s = \langle w^s \rangle + w^{s\prime}. \tag{18}$$

Substituting Eq. (18) into Eq. (13) will result in:

$$\langle w^s \rangle \phi - \frac{1}{Re_\Delta Sc} \frac{\partial \phi}{\partial z}\Big|_{z=L_z} = -w^{s\prime}\phi\Big|_{z=L_z}. \tag{19}$$

However, the sediment concentration ϕ on the right-hand-side of the above equation is part of the solution, to make sure that the top boundary has the same accuracy in terms of

time integration, the right-hand-side term is approximated by using a second-order accurate scheme:

$$\phi^{(n*)} = \left[1 + \frac{c(n)}{c(n-1)}\right]\phi^{(n-1)} - \frac{c(n)}{c(n-1)}\phi^{(n-2)}\Big|_{z=L_z}, \tag{20}$$

where n denotes the time steps, and $c = \{dt/6, 5dt/24, dt/8\}$ is the coefficient for the diffusion term in the third-order low-storage Runge-Kutta method with dt being the time-step (*Yu et al.*, 2013). In this study, the constant time step is chosen based on the Courant-Friedrichs-Lewy (CFL) criterion. $\phi^{(n*)}$ is the approximation of ϕ at the bottom at the n step, and $\phi^{(n-1)}$ and $\phi^{(n-2)}$ are sediment concentration at the previous two time steps $(n-1)$ and $(n-2)$, respectively.

4 Model Results

With the erosion/deposition boundary condition for sediment concentration, the sediment availability becomes a part of the solution. *Cheng et al.* (2015a) has demonstrated that at a given wave condition, where the free-stream velocity is $\widetilde{U}_0 = 0.56$ m/s and wave period $\widetilde{T} = 10$ sec, the transport of fine sediment with a settling velocity of about $\widetilde{W}_{s0} = 0.5$ mm/s shows three distinct characteristics, ranging from the well-mixed transport (mode I), two-layer like transport with the formation of lutocline (mode II) and laminarized transport (mode III) as the critical shear stress of erosion reduces. Moreover, reductions in the settling velocity also yield similar transitions of transport modes. In general, the settling velocity is a flow variable due to the hindered settling and the particle inertia. It has been shown that for a typical wave condition in continental shelves, the particle inertia effect is very minor although it tends to further attenuate turbulence (*Cheng et al.*, 2015b). On the other hand, for non-cohesive sediment with a relatively high reference concentrations, the hindered settling effect also plays a relatively minor role in the fine sediment transport in the wave boundary layer, while for flocs with lower gelling concentrations, the hindered settling effect can sustain a large amount of suspended sediment load and results in the laminarized transport (mode III). More scientific details of these studies can be found in *Cheng et al.* (2015a,b). The purpose of this report is to select a couple of simulations carried out in *Cheng et al.* (2015a,b) as examples in order to illustrate model input/output, model capability and to demonstrate the sensitivity of model results.

Table 1: List of simulations presented in this study.

Case	$\tilde{\tau}_c$(Pa)	W_{s0}	$\tilde{W}_{s0}(mm/s)$	St	ϕ_{ref}	$\overline{\Phi}_{eq}$	Transport mode
0	NA	NA	NA	NA	NA	NA	NA
1	0.01	9.0×10^{-4}	0.5	NA	NA	6.2×10^{-4}	III
2	0.02	9.0×10^{-4}	0.5	NA	NA	1.76×10^{-3}	II
3	0.6	9.0×10^{-4}	0.5	NA	NA	4.9×10^{-5}	I
4	0.02	3.0×10^{-4}	0.17	NA	NA	3.1×10^{-3}	III
5	0.02	18×10^{-4}	1.0	NA	NA	6.9×10^{-4}	II
$2A$	0.02	9.0×10^{-4}	0.5	0.03	NA	1.8×10^{-3}	II
$2B$	0.02	9.0×10^{-4}	0.5	NA	0.63	1.95×10^{-3}	II

The seven cases associated with the same wave condition as *Cheng et al.* (2015a,b) are presented here and they are summarized in Table 1. The Stokes Reynolds number is calculated to be Re_Δ=1000, which is in the range of intermittently turbulent flow where fully turbulent condition can only be attained for a portion of the wave cycle (e.g., *Jensen*

et al., 1989; *Ozdemir et al.*, 2014). The computational domain (see Fig. 1) is kept the same as the previous studies of *Ozdemir et al.* (2010) and *Yu et al.* (2014), which is $\widetilde{L}_x \times \widetilde{L}_y \times \widetilde{L}_z = 60\widetilde{\Delta} \times 30\widetilde{\Delta} \times 60\widetilde{\Delta}$, and it has been shown to be sufficient to resolve the largest turbulent eddies. Following *Yu et al.* (2014) and *Cheng et al.* (2015a), the model domain is discretized into $N_x \times N_y \times N_z = 128 \times 128 \times 257$ with uniform grids in both streamwise and spanwise directions, and Chebyshev collocation points are used in the vertical direction. This discretization has been verified to be sufficient to resolve turbulent scales. Taking the advantage of the statistical homogeneity in the streamwise (x) and spanwise (y) directions, ensemble-averaged (turbulence-averaged) flow quantities can be calculated approximately by averaging over the x-y plane. The Schmidt number is chosen to be $Sc = 0.5$ by following the previous studies of *Ozdemir et al.* (2010) and *Yu et al.* (2014). In this report, $\tilde{m}_e$ is assumed to be constant and its dimensional value is specified to be 3.05×10^{-7} m/s for all the cases, and the selected values of $\tilde{\tau}_c$ range from 0.01 to 0.6 Pa in order to study the effect of critical shear stress on a diverse range of transport characteristics, and $\tilde{\tau}_c$ is kept constant in each simulation.

In all the numerical simulations in Table 1, the initial condition for fluid flow is chosen to be the fully-developed clear fluid oscillatory flow of $Re_\Delta = 1000$ (Case 0 in Table 1) for each numerical simulation. Once the bottom stress exceeds the threshold value of erosion, sediments are then suspended from the bottom boundary following Eq. (16). Meanwhile, sediments will deposit to the bottom through Eq. (15). The net flux through the bottom boundary adjusts the total amount of sediment in the domain and if the wave forcing condition remains unchanged, a statistical equilibrium can be reached where the time-averaged net sediment flux over one wave period eventually become zero, or $\overline{\tilde{E}} = \overline{\tilde{D}}$, where '$\overline{\ }$' represents wave-averaged quantities, i.e., time average over one wave cycle.

4.1 Transport Modes Under Different Critical Shear Stress of Erosion

In the studies of *Cheng et al.* (2015a), the inertia terms associated with the particle Stokes number St in the particle velocity expression (Eq. (9)) are neglected by assuming that the Stokes number St is sufficiently small, and the particle velocity is calculated as:

$$u_i^s = u_i - W_{s0}\delta_{i3}. \tag{21}$$

Hence, by specifying $\widetilde{W}_{s0} = 0.5$ mm/s (or $W_{s0} = 9 \times 10^{-4}$), these simulations can be interpreted as corresponding to fine silt (no flocculation) with a particle size of $\widetilde{d} = 24$ μm and the specific gravity is $s = 2.65$. According to *Cheng et al.* (2015a), the critical shear stress of erosion $\tilde{\tau}_c$ plays a key role in controlling the sediment availability and hence

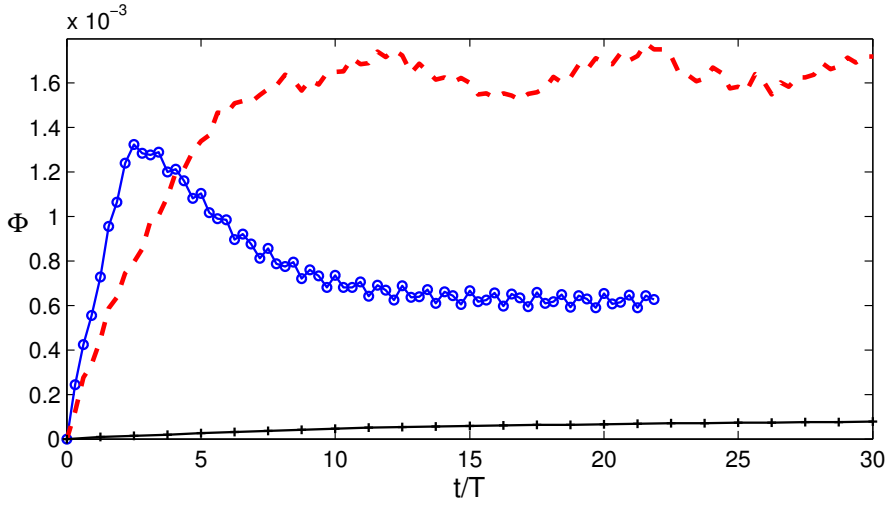

Fig. 2: Time series of the domain-averaged sediment concentration for Case 1 (curve with circle symbols), Case 2 (dashed curve), Case 3 (curve with plus symbols)

the resulting transport characteristics. This is demonstrated here by comparing Cases 1-3, where all the flow parameters are kept the same, except for the critical shear stress of erosion $\tilde{\tau}_c$ (see Table 1). Fig. 2 shows the temporal variation of the domain-averaged suspended sediment concentration, which is defined as:

$$\Phi = \frac{1}{L_z}\int_0^{L_z} \langle \phi \rangle dz. \tag{22}$$

We can see that a lower critical shear stress generally leads to a higher Φ in the domain except for Case 1. When the domain-averaged sediment concentration increases to about $\Phi = 1.3\times10^{-3}$ in Case 1, a decrease in Φ is observed after the third cycle. Due to the rapid resuspension associated with the low critical shear stress, the flow turbulence in Case 1 is completely attenuated after a couple of wave cycles, and flow eventually becomes laminar. For Cases 2-3, the corresponding $\tilde{\tau}_c$ is larger and the amount of resuspended sediment from the bottom at the initial stage increases more gradually (see Fig. 2). As we will demonstrate next, the flows are still turbulent and the domain-averaged sediment concentrations keep increasing until a quasi-equilibrium state (an equilibrium balance between the erosion flux $\overline{E}$ and the settling flux $\overline{D}$) has been reached. Hereby, the domain-averaged sediment concentration at the quasi-equilibrium state will be referred to as sediment availability $\overline{\Phi}_{eq}$ (see Table 1).

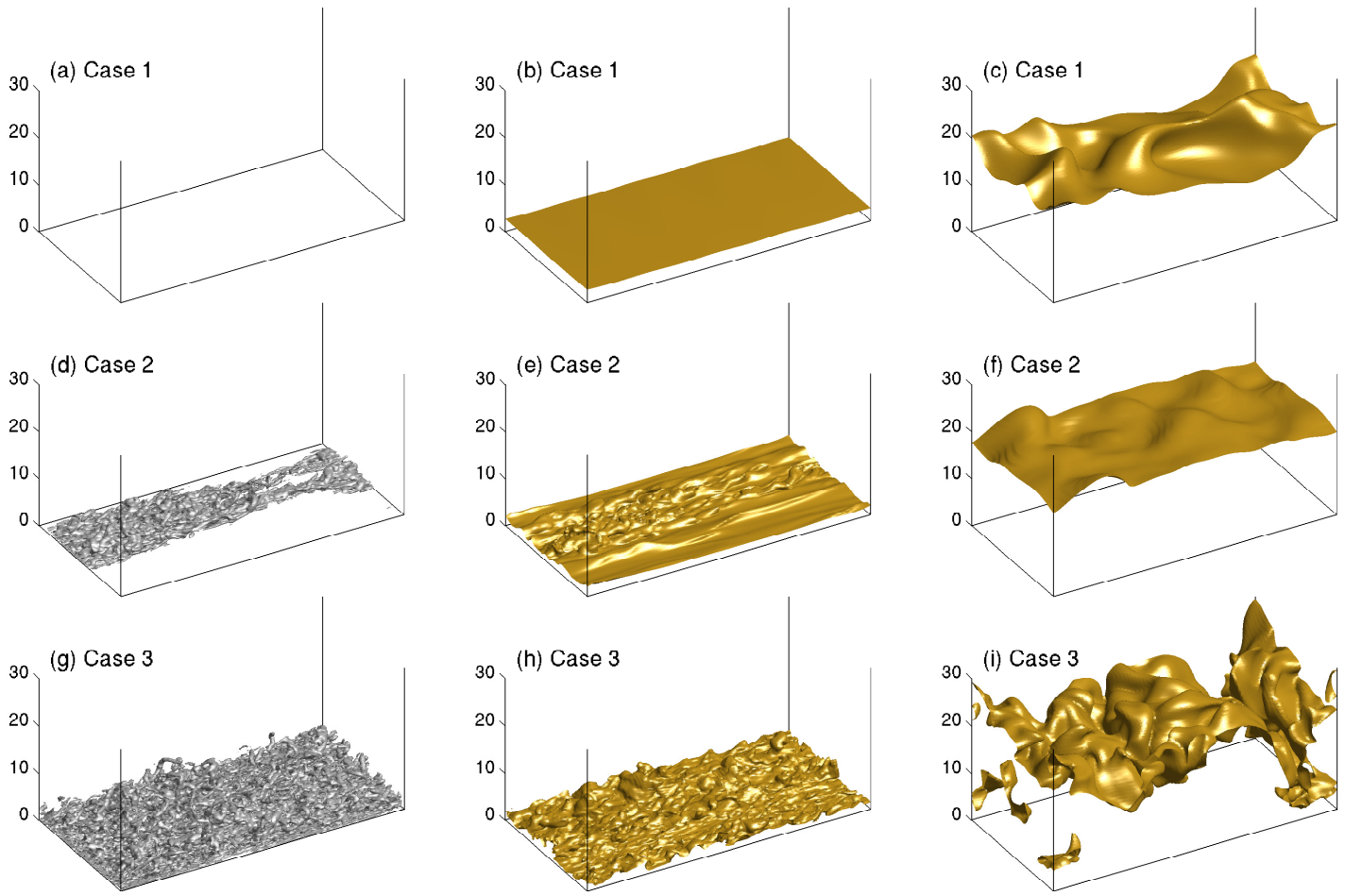

Fig. 3: Swirling strength (λ_{ci}) at flow peak ($\omega t = 0$)(a) Case 1, (d) Case 2 and (g) Case 3. The contour level used here is 5% of the maximum λ_{ci} value in Case 3. (b), (d) and (h) show the corresponding iso-surface of near-bed sediment concentration. The contour level is chosen to be the average concentration at $z = 2.5$ with $\phi = 0.005, 8.2\times10^{-3}, 9.2\times10^{-5}$ for Case 1, Case 2 and Case 3, respectively. (c), (f) , (i) show the corresponding iso-surface of sediment concentration in the middle of the domain at flow peak. The contour level is chosen to be the average concentration at $z = 20$ with $\phi = 2.2 \times 10^{-5}, \phi = 6.8 \times 10^{-4}, 7.6 \times 10^{-5}$ for Case 1, Case 2 and Case 3, respectively.

To further demonstrate sediment-turbulence interaction, the turbulence structures under different critical shear stresses for Case 1, 2 and 3 are illustrated by the iso-surfaces of local swirling strength (λ_{ci}) during flow peak (see Fig. 3 (a),(d),(g)). λ_{ci} is the imaginary part of the complex eigenvalue of the velocity gradient tensor and its magnitude can be used to quantify the strength of local swirling motion (*Zhou et al.*, 1999). In Cases 2 and 3 (see Fig. 3 (d) and (g)), some vortex structures are clearly observed over a portion of the bed. However, for Case 1 with the lowest critical shear stress of 0.01 Pa, no vortex structure is observed (see Fig. 3(a)). Meanwhile, the corresponding iso-surfaces of concentration are also shown in Fig. 3 (b) to (i). To better illustrate the resulting sediment concentration field near the bed (or in the middle of the domain), the contour level for concentration iso-surface in Fig. 3 (b), (e) and (h) (or (c), (f) and (i)) is chosen to be the plane-averaged concentration at $z = 2.5$ (or $z = 20$) in each case. Since there are no turbulent coherent structures observed in Case 1 (Fig. 3(a)), a flat near-bed iso-surface of concentration field is obtained in Fig. 3(b). However, irregular structures of very dilute concentration can still be observed at around $z = 20$ due to turbulence from the top half domain (see Fig. 3(c)). As the critical shear stress is increased to 0.02 Pa in Case 2, sparse coherent vortex structures can be observed over a portion of the near-bed region (see Fig. 3(d)). This region is corresponding to a stripe of more irregular/chaotic sediment concentration structures shown in Fig. 3(e). In the middle of the channel at $z = 20$ (see Fig. 3(f)), the iso-surface of sediment concentration is much less chaotic, which suggests a much weaker turbulence. As the critical shear stress is further increased to 0.6 Pa in Case 3, it is evident that the turbulence near the bed is much stronger with denser near-bed turbulent structures (see Fig. 3(g)). In this case, the iso-surface of sediment concentration in the middle of the domain (at $z = 20$, see Fig. 3(i)) is similarly chaotic, suggesting that turbulence is sufficiently large throughout the domain. Comparing to iso-surface of sediment concentration in Case 2, it is clear that fluctuations in sediment concentration are much stronger in Case 3 (Fig. 3(i)), implying that the turbulence in Case 2 is significantly suppressed in the middle of the domain despite the flow remains turbulent near the bed.

Turbulence-averaged flow statistics, namely the sediment concentration, streamwise velocity and turbulent intensity during flow peak for Case 1, 2 and 3 are shown in Fig. 4. Because the flow is statistically homogeneous in the streamwise and spainwise directions, turbulence-averaged quantities are computed by averaging over the xy-plane. For a better illustration, only the bottom half channel ($z = 0 \sim 30$) is shown here. Several distinct features can be observed from the concentration profiles (Fig. 4(a)). Firstly, sediment concentration profile of Case 3 is relatively uniform throughout the lower half of the domain and although not shown here, the profiles of turbulent intensity and streamwise velocity in Case 3 is almost identical to those of the clear fluid condition (Case 0), this flow feature is quite similar to a well-mixed condition (regime I) that was previously reported by

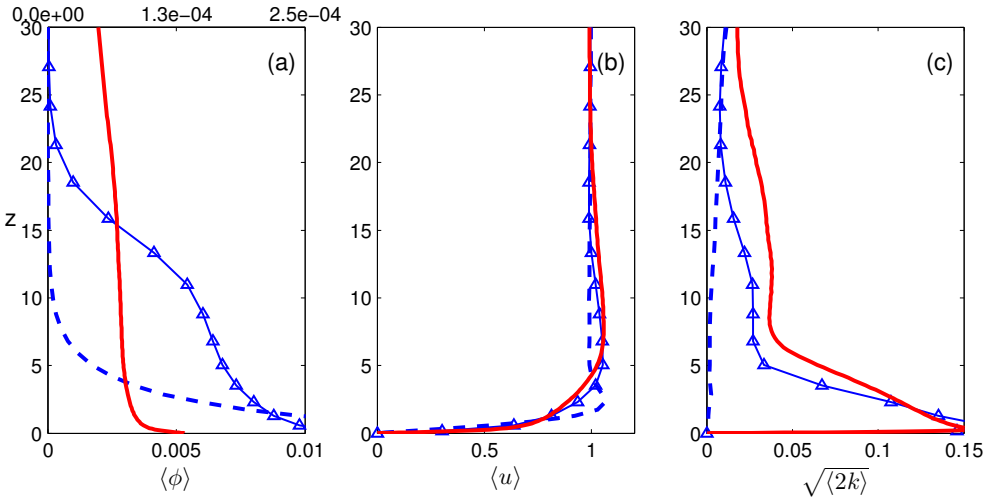

Fig. 4: Ensemble-averaged profiles of (a) sediment concentration, (b) non-dimensional streamwise velocity and (c) non-dimensional turbulence intensity during flow peak ($\omega t = 0$) for Case 1 (dashed curve), Case 2 (curve with triangle symbol), Case 3 (solid curve); In (a), the top x-axis is the concentration scale for Case 3, and the bottom axis is the concentration scale for Case 1 and Case 2.

Ozdemir et al. (2010). Distinctly, A nearly exponential sediment concentration profile (see Fig. 4(a)) can be observed in Case 1, in which a high sediment concentration only accumulates very close to the bed and decays rapidly away from the bed. This sharp decrease of concentration is clearly associated with the strongly suppressed turbulent intensity (see Fig. 4 (c)) throughout the lower half of the channel. Meanwhile, the streamwise velocity profile in Fig. 4(b) is distinct from those of Case 2 and 3, and a reduction of boundary layer thickness is observed. Flow features presented here are consistent with the regime IV reported by *Ozdemir et al.* (2010), where the flow is completely laminarized by a large availability of sediment. For Case 2, a relatively sharp negative gradient of sediment concentration (lutocline) can be seen around $z = 10 \sim 15$, while this feature is absent in Case 1 and Case 3. A classic two-layer feature is characterized by the lutocline, which separates the upper quasi-laminar layer from the lower turbulent layer. Such feature can be clearly seen in the profiles of turbulent intensity shown in Fig. 4 (c). Below $z = 10$, the turbulent intensity of Case 2 is comparable to that of Case 3 (or the clear fluid condition). However, the turbulent intensity above $z = 15$ is less than 50% of that in Case 3. The two-layer-like features of Case 2 are consistent with the regime II reported by *Ozdemir et al.* (2010) for moderate sediment availabilities.

Based on the results presented so far, it is evident that the present turbulence-resolving

numerical model is able to study different transport characteristics due to different critical shear stress of erosion. By varying the critical shear stress of erosion, three transport modes, which are similar to the flow regimes I, II and IV described by *Ozdemir et al.* (2010) are observed. It is found that under the Stokes Reynolds number $Re_\Delta = 1000$, very low critical shear stress (very high erodibility) as low as 0.01 Pa can cause significant turbulence suppression by sediment induced stable density stratification that further leads to laminarized flow (transport mode III). Interestingly, slightly increased critical shear stress ($\tilde{\tau}_c \geq 0.02$ Pa) causes lower sediment availability, much less turbulence attenuation and the formation of lutocline that separates the turbulent layer from the upper quasi-laminar layer (transport mode II). When the critical shear stress is sufficiently large ($\tilde{\tau}_c \geq 0.6$ Pa), the sediment availability is very low such that the effect sediment-induced density stratification on the turbulence is negligible (transport mode I).

4.2 Transport Modes Under Different Settling Velocities

To be consistent with the study of transport modes under different critical shear stresses of erosion $\tilde{\tau}_c$, the particle velocity is calculated in the same manner as Case 1-3, i.e., Eq. (21) is used. *Cheng et al.* (2015a) also demonstrated that the settling velocity is critical in controlling the sediment availabilities and thus the resulting turbulence attenuation. In this section, the capability of the model to study the effect of different settling velocities are presented. While the settling velocity is kept constant in each simulation, a range of settling velocity between $0.17 \sim 1.0$ mm/s is considered in Cases 2, 4 and 5 (see Table 1), and this range of settling velocity is typical for fine sediment in the field condition (e.g., *Hill et al.*, 2000). The critical shear stress of erosion is kept the same, $\tilde{\tau}_c = 0.02$ Pa.

Fig. 5 compares profiles of the turbulence-averaged concentration, the streamwise velocity and the turbulent intensity for cases with a small (Case 4), medium (Case 2) and large (Case 5) settling velocity (see Table 1). By keeping the critical shear stress constant, it is shown here that different transport modes are realized with different settling velocities. To better illustrate the differences, sediment concentrations are normalized by the domain-averaged sediment concentration. As discussed previously, Case 2 with $\tilde{W}_s = 0.5$ mm/s corresponds to transport mode II. Decreasing the settling velocity to $\tilde{W}_s = 0.17$ mm/s in Case 4 shows a significantly different concentration profile (Fig. 5 (a)). The lutocline is not present in the concentration profile of Case 4 and it is clear from Fig. 5 (c) that flow turbulence in Case 4 is completely suppressed, which indicates that the laminarized transport mode III is observed in Case 4.

On the other hand, increasing the settling velocity from $\tilde{W}_s = 0.5$ mm/s to $\tilde{W}_s = 1.0$ mm/s (Case 5) still produces the transport mode II (see Fig. 5). However, there is a slight increase in the lutocline elevation. In Case 2, the lutocline is located at around $z = 13$,

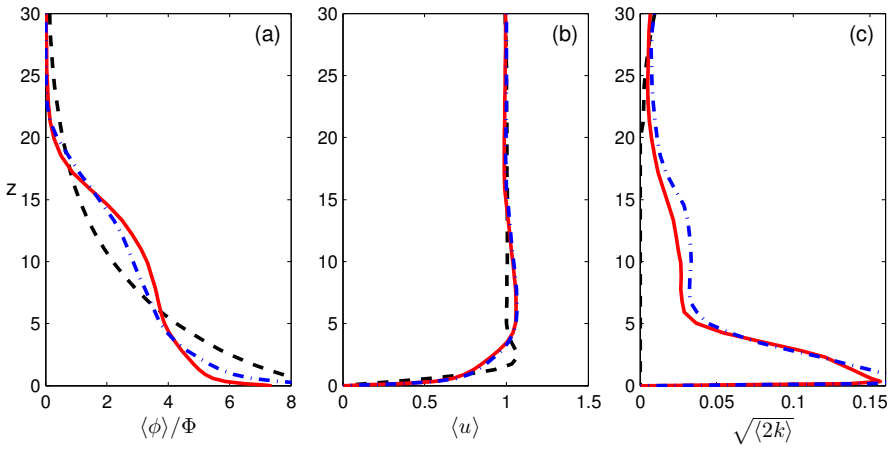

Fig. 5: Ensemble-averaged profiles of (a) sediment concentration, (b) non-dimensional streamwise velocity and (c) non-dimensional turbulence intensity during flow peak ($\omega t = 0$) for Case 2 (solid curves), Case 4 (dashed curves) and Case 5 (dash-dotted curves).

while increasing the settling velocity twice (Case 5), the lutocline moves upward to about $z = 16$. Moreover, the turbulent intensity above $z = 5$ in Case 5 is also larger. By examining the sediment availability (see $\overline{\Phi}_{eq}$ in Table 1), it is clear that Case 5 with a larger settling velocity has a much lower sediment availability. Hence, the higher lutocline location and stronger turbulence (weaker turbulence attenuation) in Case 5 can be explained by the lower sediment availability. In contrast, laminarized transport mode III, Case 4, is caused by the high sediment availability and the significant turbulence attenuation.

4.3 Effect of Particle Inertia

To include the effect of the particle inertia, the sediment velocity is calculated by retaining the first-order inertia term in Eq. (9):

$$u_i^s = u_i - W_{s0}\delta_{i3} - St(1 - \frac{1}{s})\frac{Du_i}{Dt}, \tag{23}$$

Here we demonstrate the particle inertia effect by comparing with the baseline Case 2 (see Table 1). For Case 2, the particle response time and characteristic time scale of the flow are $\widetilde{t}_p = 8.5 \times 10^{-5}$ s and $\widetilde{t}_l \approx 3.2 \times 10^{-3}$ s, respectively. The resulting Stokes number is $St = \widetilde{t}_p/\widetilde{t}_l = 0.03$, which is much smaller than unity. Except for the difference in the particle velocity expressions, other flow and sediment parameters in Case 2 and Case 2A are kept the same, and thus any difference between these two cases is due to the extra inertia term in the particle velocity expression.

The effect of the particle inertia is shown by comparing the ensemble-averaged profiles (see Fig. 6) of sediment concentration, non-dimensional streamwise velocity and non-dimensional turbulent intensity for Case 2 (inertia effect neglected) and Case 2A (St=0.03).

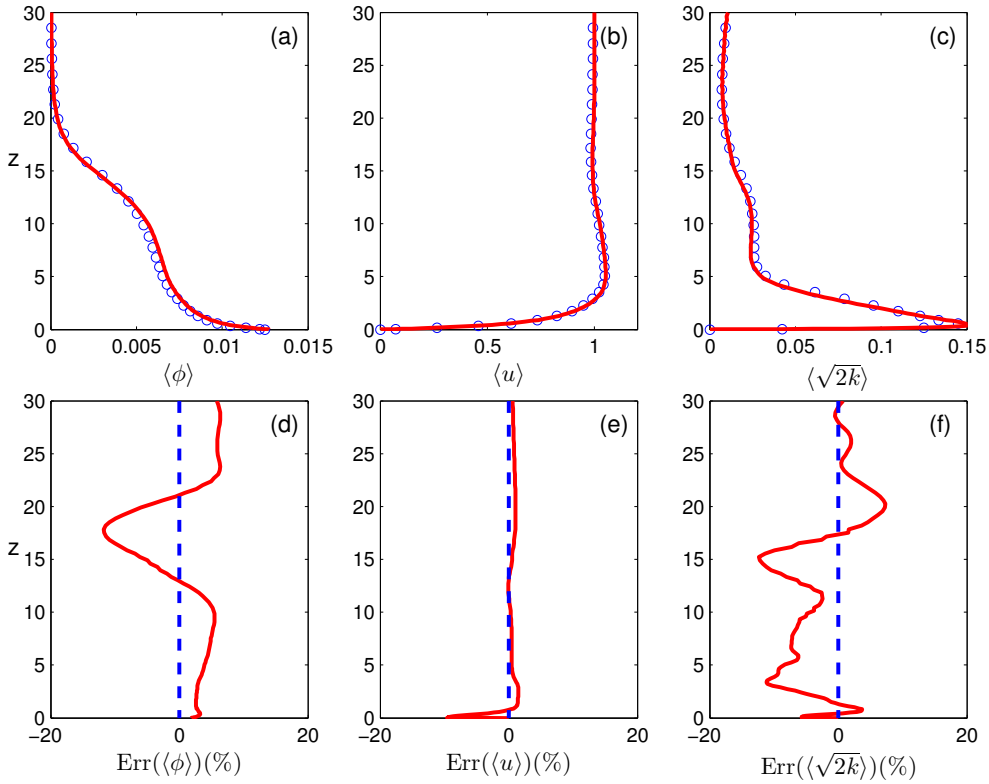

Fig. 6: Comparison of the ensemble-averaged profiles of (a) sediment concentration, (b) streamwise velocity and (c) turbulence intensity during flow peak ($\omega t = 0$) for Case 2 (circle symbol), Case 2A (solid curve); The relative difference (%) of these flow quantities are shown in (d), (e) and (f), respectively; The dashed lines denotes the level of zero error.

It is reminded here that Case 2 belongs to transport mode II, in which the lutocline separates the upper quasi-laminar layer from the lower turbulent layer. In this case, the lutocline is located approximately at $z = 13 \sim 14$ (see the solid curve Fig. 6(a)). By including the first-order inertia term, the resulting sediment concentration profile (see Fig. 6(a)) is very similar to that of Case 2. Moreover, the relative difference of the sediment

concentration is shown in Fig. 6(d), which is defined as:

$$Err(\langle\phi\rangle) = \frac{\langle\phi_{2A}\rangle - \langle\phi_2\rangle}{\langle\phi_2\rangle} \times 100\%, \tag{24}$$

where $\langle\phi_2\rangle$ is the plane-averaged sediment concentration in Case 2, and $\langle\phi_{2A}\rangle$ is the plane-averaged sediment concentration in Case 2A. The relative difference of the streamwise velocity $Err(\langle u\rangle)$ and the turbulent intensity $Err(\langle\sqrt{2k}\rangle)$ can be calculated in a similar manner. We can see that the overall relative difference is small ($< 10\%$). A reduction of sediment concentration can be observed in the range of $13 < z < 21$, and the peak difference appears at around $z = 18$ (about -10%), which is close to the lutocline. On the contrary, sediment concentration below $z = 13$ is increased by about 7%. This observation suggests the lowering of lutocline when inertia effect is considered. Meanwhile, the streamwise velocity (see Fig. 6(b)) of both cases are again very similar, and the relative difference (see Fig. 6(e)) is generally smaller than 5%, and the peak value can be observed near the bottom. Furthermore, comparison of turbulence intensity is shown in Fig. 6(c). Although the turbulence intensity profiles from Case 2 and Case 2A are also very close, it is evident that the predicted turbulence is slightly lower by including the inertia effect with the peak attenuation occurs at around $z = 15$ near the lutocline. More attenuated turbulence is consistent with lowered lutocline (*Ozdemir et al.*, 2011).

Moreover, the relative differences in effective settling velocity at three representative instants are discussed in Fig. 7. The relative difference in the effective settling velocity is calculated by the ensemble-average of the additional term associated with the inertia effect normalized by W_{s0}:

$$Err(\langle W_s\rangle) = St(1 - \frac{1}{s})\frac{\langle\frac{Dw}{Dt}\rangle}{W_{s0}} \times 100\% \tag{25}$$

In Fig. 7(a), the wave phase (ωt) is defined such that $\omega t = 0$ ($\omega t = \pi$) corresponds to the positive (negative) peak of free-stream velocity, and $\omega t = \pi/2$ and $3\pi/2$ correspond to flow reversals. From the comparison of effective settling velocities (Fig. 7(b,c,d)), we can see that the effective settling velocity is nearly unaffected above $z = 20$ due to very low turbulence above the lutocline. Between $1.5 < z < 20$, including the particle inertia reduces the effective settling velocity. However, the reduction is only within 3%. Moreover, an increase of the effective settling velocity can be observed near the bottom $0 < z < 1.5$, and the peak value of the increment is about 5% at flow peak. However, the effective settling velocity at the bottom is still reduced by about 2%. As the flow decelerates to $\omega t = \pi/3$, the increment of effective settling velocity at around $z = 1.5$ is decreased to about 1%. After the flow reserves and accelerates to $\omega t = 2\pi/3$, a uniform reduction of effective settling velocity can be observed below the lutocline, and the reduction is less than 2%. Overall, the inertia effect slightly reduces velocity fluctuation in the z-direction

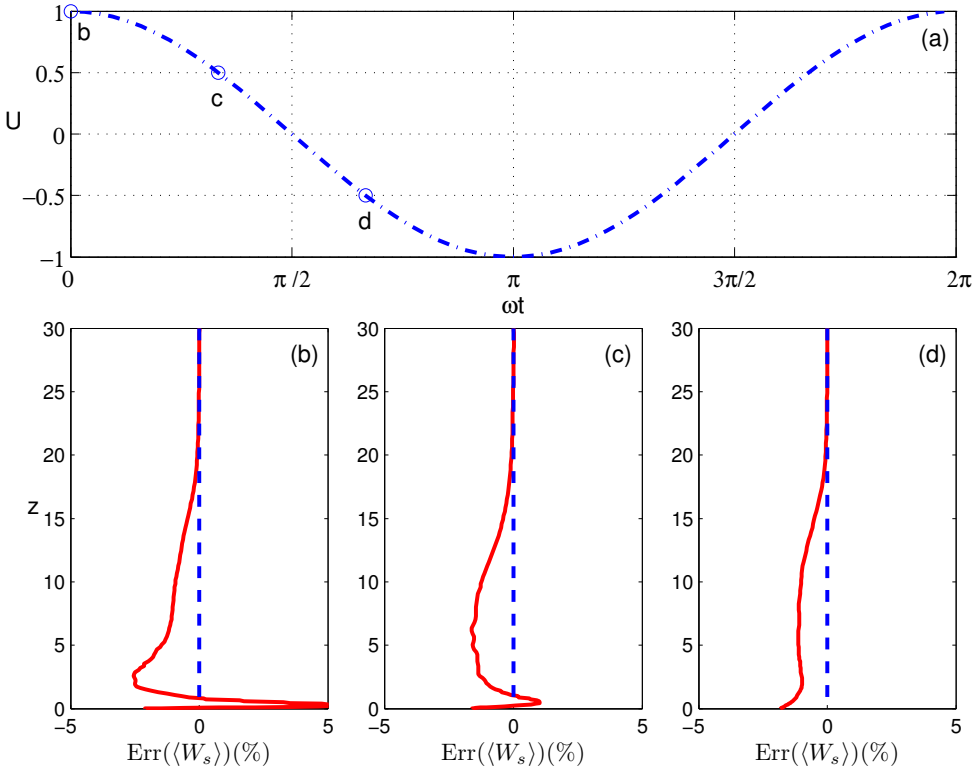

Fig. 7: (a) Time series of free-stream velocity $U(t)$. Three representative instants (b,c,d) are shown with open circles. The relative difference ($\%$, solid curve) of effective settling velocities between Case 2 and Case 2A at these three representative instants are shown in (b) flow peak ($\omega t = 0$), (b) $\omega t = \pi/3$ and (d) $\omega t = 2\pi/3$; The dashed lines denotes the level of zero error.

and hence the Reynolds stress is reduced (not shown here for conciseness). This can further lead to a reduction of turbulent production and hence more attenuation of turbulence. However, the Stokes number considered here remains to be too small ($St = 0.03$) to trigger the transition to transport mode III.

As discussed in this section, the particle inertia effect can be included by retaining the first order St term in the particle velocity expansion in our numerical model. Based on Case 2 with $St = 0.03$, the inertia effect is demonstrated to be small on concentration profiles, velocity profiles and turbulent intensity. This negligible effect is consistent with the small $Err(\langle W_s \rangle)$ which is generally within 5%.

4.4 Effect of Hindered Settling

To incorporate the effect of hindered settling, the particle velocity is expressed to account for the hindered settling correction:

$$u_i^s = u_i - W_{s0} f(\phi) \delta_{i3}, \tag{26}$$

where the dimensional Stokes settling velocity $\widetilde{W}_{s0}$ is calculated by Eq. (2). In our numerical model, the hindered settling function $f(\phi)$ is introduced to correct the settling velocity, and the model of *Richardson and Zaki* (1954) is chosen:

$$f(\phi) = \big(1 - \frac{\phi}{\phi_{ref}}\big)^m, \tag{27}$$

where ϕ_{ref} is the reference concentration, i.e., a maximum packing concentration (*Richardson and Zaki*, 1954; *Mehta*, 1986; *Dankers and Winterwerp*, 2007). Clearly, the degree of hindered settling and hence the resulting transport is highly dependent on ϕ_{ref}. For non-cohesive sediments, ϕ_{ref} corresponds to the maximum packing limit, which around $\phi_{ref} = 0.63$, at which the mean distance between the edges of the nearest neighbors is nearly zero (*Berryman*, 1983). Here, we present the case with a reference concentration associated with non-cohesive particles (see Case 2B in Table 1). The empirical exponent m is related to the particle Reynolds number ($Re_p = \widetilde{W}_{s0}\widetilde{d}/\nu$):

$$m = \begin{cases} 4.6, & Re_p \leq 0.2 \\ 4.4 Re_p^{-0.03}, & 0.2 < Re_p \leq 1 \\ 4.4 Re_p^{-0.1}, & 1 < Re_p \leq 500 \\ 2.39, & Re_p > 500 \end{cases}. \tag{28}$$

The ensemble-averaged flow statistics in Case 2 and Case 2B are compared in Fig. 8 to study the effect of the hindered settling for non-flocculated condition ($\phi_{ref} = 0.63$). Case 2 and Case 2B show a similar feature of concentration profiles (Fig. 8(a)). Since the lutoclines are observed in both Case 2 and Case 2B near $z = 14$, transport mode II is also obtained for Case 2B. However, Case 2B shows slightly more sediment below the lutocline. Although the increase is within 20%, this notable increment of total load in the domain is clearly associated with the reduced settling velocity. Meanwhile, the streamwise velocity profiles (see Fig. 8(b)) show that the overshoot near the bottom in Case 2B is slightly larger (within 10%) than that of Case 2. Below the lutocline, the turbulent intensity in Case 2B is consistently lower that that of Case 2 by about 5% to 20% (see Fig. 8(f)). When settling velocity is effectively reduced by hindered settling effect, more sediments are suspended in the domain (*Cheng et al.*, 2015a), which leads to an

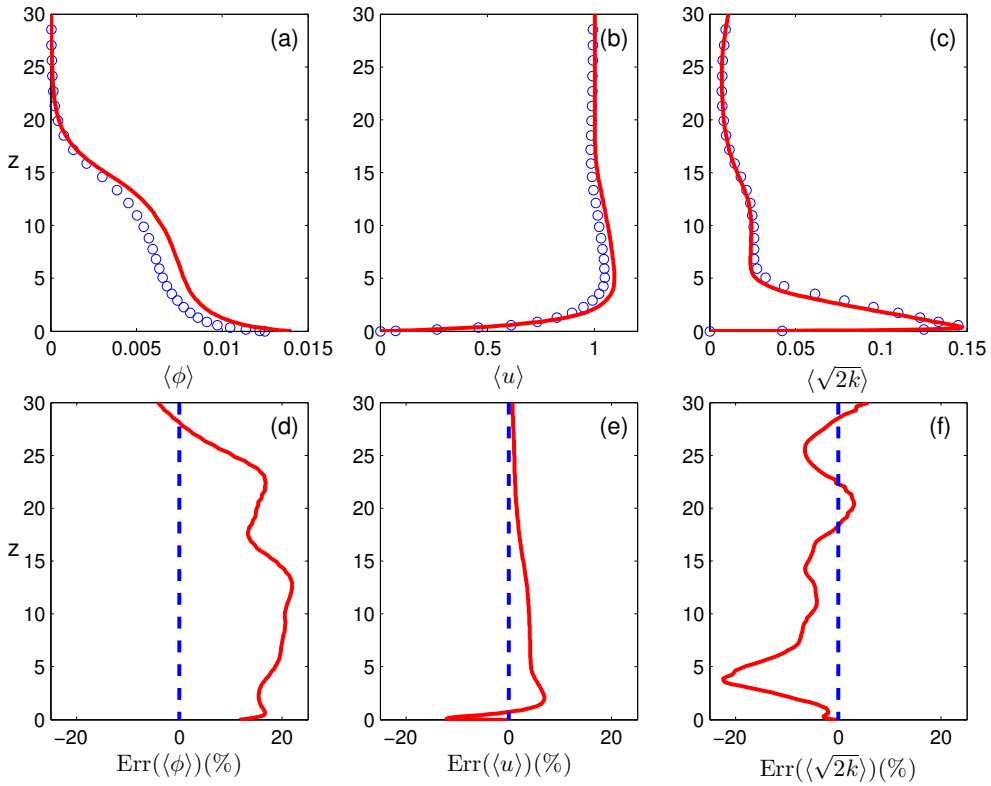

Fig. 8: Comparison of the ensemble-averaged profiles of (a) sediment concentration, (b) streamwise velocity and (c) turbulence intensity during flow peak ($\omega t = 0$) for Case 2 (circle symbols), Case 2B (solid curve); The relative difference (%) of these flow quantities are shown in (d), (e) and (f), respectively; The dashed lines denotes the level of zero error.

enhanced sediment-induced density stratification and a stronger attenuation of turbulence is observed.

Fig. 9 presents the normalized effective settling velocity, which is defined as the difference between the sediment velocity and the fluid velocity in the z-direction normalized by the Stokes settling velocity. Since the features are similar during the entire wave cycle, only the comparison at the flow peak is discussed here. We can see that hindered settling renders a reduction in the effective settling velocity, and the reduction of effective settling velocity is larger near the bottom, where the sediment concentration is larger. For Case 2B ($\phi_{ref} = 0.63$), the reduction is less than 10% near the bottom. This reduction is consistent with the enhanced sediment availability, as well as the resulting stronger turbulence attenuation.

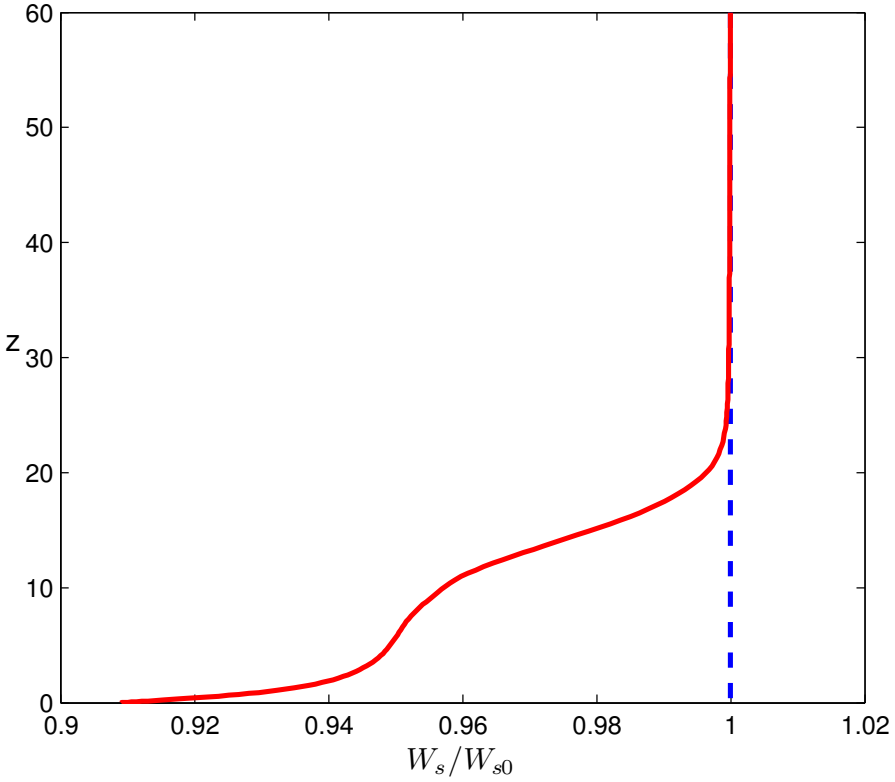

Fig. 9: Normalized effective settling velocity profile for Case 2 (dashed curve), Case 2B (solid curve) during flow peak ($t = 15T$).

5 Conclusion and Future Work

A 3D turbulence-resolving numerical model for fine sediment transport in the bottom boundary layer has been developed. The numerical model has the capability to simulate fine sediment transport using two different approach for sediment availability, namely, the prescribled sediment availability and the erosional/depositional bottom boundary. This report further discusses simulation results using erosional/depositional bottom boundary option. The transport mode of fine sediment due to critical shear stress of erosion and settling velocities is successfully studied using this model, and model results reveal the existence of three transport modes, namely, the dilute suspension in well-mixed condition (transport mode I), the formation of lutocline due to moderately attenuated turbulence by sediment-induced stable density stratification (transport mode II), and laminarized flow due to a significant turbulence attenuation (transport mode III) (see more details in *Cheng et al.* (2015a)).

Meanwhile, the model provides flexible options for the sediment phase velocity, and particle inertia and hindered settling for fine sediment can be included. Though it is revealed that at the Stokes number of $St = 0.03$, which corresponds to the value typical of fine sediment transport in energetic continental shelves, the particle inertia makes a very minor difference. More attenuation of turbulence is observed by considering the particle inertia at $St = 0.03$. It is interesting to further consider other flow conditions and sediment properties, where the Stokes number is larger. Furthermore, the hindered settling effect can be incorporated by using the model of *Richardson and Zaki* (1954). Only non-flocculated sediment with ϕ_{ref}=0.63 is presented in this report. *Cheng et al.* (2015b) showed that by varying the reference concentration when floc properties are considered, more significant hindered settling effect (lower reference concentrations) enhances sediment availability, significantly attenuate flow turbulence and the laminarized transport mode III is obtained. Moreover, interesting phenomenon such as gelling ignition (*Kampf and Myrow*, 2014; *Cheng et al.*, 2015b), where an unlimited increase of sediment in the domain, can be obtained when the reference concentration is low enough.

Future extension of the present numerical model can be carried out in several directions. The effect of current in the wave boundary layer should be investigated. Moreover, mixed grain size transport and bedform should be further studied to investigate their effect on the resulting fine sediment transport mode.

6 Appendix

6.1 Installation and Compilation

FineSed3D is distributed in a compressed file, FineSed3D.tar. To install the programs, first, uncompress the package by using the command:

```
tar -xvf FineSed3D.tar
```

to extract files from the uncompressed package. The exacted files will be distributed in three new directories: /Examples, /Src and /User_Manual.

Before compilation, make sure the Intel Math Kernel Library (MKL) and FFTW packages are successfully installed. For more informations about these libraries, please go to:

```
For MKL, go to: https://software.intel.com/en-us/intel-mkl
For FFTW, go to: http://www.fftw.org/
```

After installing the MKL and FFTW libraries, we can start to compile the numerical model. First go to /Src and modify Makefile if needed. There are several necessary flags in Makefile needed to specify below:

-EXEC: the name of executable command to be generated after compilation.

-TGZFILE: the name of the compressed file.

-INC: all the include files, which defines global variables, and mesh information.

-OBJS: the rule of generating the names of object files.

-MKL_HOME: define the directory of mkl library.

-MKLIBS: define the library links for mkl.

-FLAGS: define code debug flags.

-DEBUGFLAGS: define flags for code debug.

-OPTFLAGS: define optimization option for compilation, use -O2 for optimization level 2.

-MPFLAGS: define parallelizatino library, use -openmp for openmp library.

-FCMP: define the include files for FFTW library.

-FCSP: define the include files for FFTW library.

Meanwhile, the number of mesh grid points in each direction is defined in **global.inc**:

```
INTEGER nx,ny,nz
PARAMETER (nx=128, ny=128, nz=257)
```

6.2 Model Input

Take the model input for the hindered settling ($\phi_{ref} = 0.63$) as an example, the following is a description of parameters in the file called **initial**, and variable names are added in brackets above each variable values, and they are not a part of initial file:

```
#MAIN
vel
(istart iters ch_fin m_fin)
2880000 8000 1 0
(oi_chan out_press limit)
8000 1 0
(oi_timer oi_cfl oi_spec oi_mean oi_gbal oi_1d)
9999999 1 99999999 9999999 24000 9999999
(re  gradpbar dt cflmax)
30000.d0 1.0 0.0001 1.0
(tt_yes twc_yes otau_yes)
1 0 1
#END_MAIN
#THRM
conc
(sc ri(or 1/Frˆ2) Tmax RR nbsq_yes md_rhs_yes)
0.5 3.264d-6 0 1.65 0 1
(ttab ttat =-w_settling)
-0.0009 -0.0009
(ttbb ttbt =-1/(re*sc))
-0.002 -0.002
(ttgb ttgt)
0.0 0.0
(w_settling tau_p beta_p rey_p phiave=1/phi_ref me tauc)
-0.0009 0.0 0.4762 0.0514 1.5873 3.05d-7 2.d-2
```

```
#END_THRM
#SP_VISC
(epssvx epssvy)
0.0 0.0
(msvx msvy)
1 1
#END_SP_VISC
```

The detailed definitions are described as follows:

vel: output name for velocity.

istart: the time step to start the simulation, if it is not 0, **ch_fin** needs to be set to 1 to read the previous files at the starting time step.

iters: number of time steps to run, in addition to the **istart**.

ch_fin: if hot start, set **ch_fin** to 1, and the output files at the time step **istart** will be read to initialize the simulation, or if cold start, set **ch_fin** to 0 for cold start, and initial perturbations are added to the prescribed velocity profile, which is defined in **initial_compact.F**.

m_fin: if cold start (ch_fin=0), to generate the initial perturbation, set to 0 if the mean velocity is zero, else set to 1 to read mean velocity from 'means.istart', where 'istart' is specified as the starting time step.

oi_chan: output interval (number of time steps).

out_press: output pressure? set to 1 for yes, or 0 for no.

limit: set the limit for output? set to 1 for yes, or 0 for no.

oi_timer: output interval for time information, set to large value if the output is not necessary.

ch_cfl: output interval for CFL number.

oi_spec: output interval for spectral information, set to large value if the output is not necessary.

oi_mean: output interval for mean values, set to large value if the output is not necessary.

oi_gbal: output interval for TKE balances, such as TKE production, TKE dissipation, etc, mode details can be found in source code **stats.F**.

oi_1d: output interval 1D average information, set to large value if the output is not necessary.

re: define Reynolds number, Re_Δ, since the vertical domain ($0 \leq z \leq 60$) is scaled to -1 to 1, the Reynolds number is scaled by 30.

gradpbar: define magnitude of mean pressure gradient, dummy, because it is redefined in **rhs.F**, since it should be function of time for oscillatory flow, however, a constant pressure gradient can be specified for steady flow.

dt: time step, dummy, redefined in **main.F**.

cflmax: allowed maximum CFL number, a value of 0.3 is recommended.

tt_yes: include sediment phase? set to 1 for yes, and sediment phase will be solved, or set to 0 for clear fluid, and sediment phase is not solved.

twc_yes: use two-way coupled formulas, set to 1 for yes, and 0 for no.

otau_yes: include particle inertia? set to 1 for yes, and the material derive of fluid velocity Du/Dt will be calculated and first order Stokes number term in the particle velocity expression (see Eq. (23)) will be calculated, meanwhile, the special treatment of top boundary condition will be adopted (see Section 3). or set to 0 to ignore inertia effect, and particle velocity will be calculated by using Eq. (21).

conc: output name for sediment concentration.

ri or 1/Fr^2: define the bulk Richardson number (Ri_{bulk}) or the particle Froude number (Fr). If no-flux boundary condition is used for the sediment concentration at the bottom boundary, then a fixed sediment availability Φ can be specified, and the bulk Richardson number Ri_{bulk} can be specified as $Ri_{bulk} = (s-1)g\widetilde{\Delta}\Phi/\widetilde{U}_0^2$. Notice that by spacifying the bulk Richardson number, the domain averaged sediment concentration is equivalently specified. If the erosion/deposition boundary condition is used for the sediment concentration at the bottom boundary, then the inverse of the square of particle Froude number is specified, and it is calculated as $1/Fr^2 = (s-1)g\widetilde{\Delta}/\widetilde{U}_0^2$. Notice that vertical domain is scaled, the bulk Richardson number and particle Froude number should be corresponding scaled.

Tmax: set to 1 if the Boussinesq approximation is disabled, and the void fraction of fluid will be included in the momentum equation for fluid phase, see **rhs.F** for more details.

RR: (s-1), where s is the specific gravity of sediment.

nbsq_yes: quit Boussinesq approximation? set to 1 for yes, or set to 0 for no.

md_rhs_yes: use right-hand-side of momentum equation to calculate material derivative of fluid velocity? set to 1 for yes, or set to 0 for no, and left-hand-side of momentum equation will be used to calculate the material derivative of fluid velocity. the material derivative will be used when the particle inertia effect is considered.

ttab, ttbb: coefficients for the sediment bottom boundary condition, $ttab = W_{s0}$, $ttbb = -1/(Re_{\Delta}Sc)$.

ttat, ttbt: coefficients for the sediment top boundary condition, $ttat = W_{s0}$, $ttbt = -1/(Re_{\Delta}Sc)$.

w_settling: Stokes settling velocity, W_{s0} (see Eq. (2)), it is define in the way that it is positive if upwards.

tau_p: Stokes number, St, similar as Reynolds number and bulk Richardson number, it shall be scaled as the domain is scaled in the numerical model.

beta_p: 1/s.

rey_p: particle Reynolds number, which is used in the hindered settling model, see Eq. (28).

phiave: 1/ϕ_{ref} for hindered settling (see Eq. (27)), set it to 0 to ignore hindered settling.

me: erosion rate coefficient m_e, non-dimensional.

tauc: critical shear stress of erosion, dimensional (Pa).

epssvx: set to greater than 0 if to use spectral viscosity in x direction.

espsvy: set to greater than 0 if to use spectral viscosity in y direction.

msvx: should be less than nx/2, used in spectral viscosity.

msvy: should be less than ny/2, used in spectral viscosity.

6.3 Model Output

Note that the executable file, initial file as well as the *.inc file from the folder /src should be present in the present working directory in order to run. The code can be run using the following command:

```
FineSed3D.x < initial
```

where FineSed3D.x is the executable file generated by the code compilation. The output files are:

vel.*: fluid velocity, binary format, the I/O format can be found in **io.F**.

conc.*: sediment concentration, binary format, see **io.F** for detailed I/O information.

press.*: fluid dynamic pressure, binary format, see **io.F** for detailed I/O information.

vel_p.*: difference of sediment velocity from fluid velocity, output if inertia effect or hindered settling effect is considered, binary format, see **io.F** for detailed I/O information.

DDt.*: material derivative of fluid velocity, output if inertia effect is included ($tau\_p > 0$), binary format, see **io.F** for detailed I/O information.

ushear.dat: time series of plane averaged bottom shear velocity, $\langle u_* \rangle = \sqrt{|\langle \widetilde{\tau}_b \rangle| / \rho^f}$, it is output every time step, ASCII format.

logfile: log of screen output to monitor the quantities such as CFL number, domain averaged concentration, bottom concentration, etc., ASCII format.

these output files are saved under the same directory of the present working directory. large output files are in binary format to save I/O time, and their format can be found in io.F in the folder of /Src. The names of the binary output files are a combination of variable name and an output time step such as vel.8000, vel.16000,....

References

Arakawa, A., and V. R. Lamb (1981), A potential enstrophy and energy conserving scheme for the shallow water equations, *Mon. Wea. Rev.*, *109*(1), 18–36.

Balachandar, S., and J. K. Eaton (2010), Turbulent dispersed multiphase flow, *Annu. Rev. Fluid Mech.*, *42*, 111–133.

Berryman, J. G. (1983), Random close packing of hard spheres and disks, *Phys. Rev. A*, *27*(2), 1053–1061.

Bever, A. J., J. E. McNinch, and C. K. Harris (2011), Hydrodynamics and sediment-transport in the nearshore of Poverty Bay, New Zealand: Observations of nearshore sediment segregation and oceanic storms, *Cont. Shelf Res.*, *31*(6), 507–526.

Byun, D.-S., and X. H. Wang (2005), The effect of sediment stratification on tidal dynamics and sediment transport patterns, *J. Geophys. Res.*, *110*(C3), C03,011.

Cantero, M. I., S. Balachandar, and M. H. Garcia (2008), An Eulerian-Eulerian model for gravity currents driven by inertial particles, *Int. J. Multiphase Flow*, *34*(5), 484–501.

Cheng, Z., X. Yu, T.-J. Hsu, C. E. Ozdemir, and S. Balachandar (2015a), On the transport mode of fine sediment in the wave boundary layer due to resuspension/deposition—a turbulence-resolving numerical investigation, *J. Geophys. Res.: Oceans, in review*.

Cheng, Z., X. Yu, T.-J. Hsu, and S. Balachandar (2015b), A numerical investigation of fine sediment resuspension in the wave boundary layer–uncertainties in particle inertia and hindered settling, *Comput. Geosci., in review*

Chorin, A. J. (1968), Numerical solution of the Navier-Stokes equations, *Math. Comput.*, *22*(104), 745–762.

Cortese, T. A., and S. Balachandar (1995), High performance spectral simulation of turbulent flows in massively parallel machines with distributed memory, *Int. J. High Perform. C.*, *9*(3), 187–204.

Dankers, P., and J. Winterwerp (2007), Hindered settling of mud flocs: Theory and validation, *Cont. Shelf Res.*, *27*(14), 1893–1907.

Fan, S., D. J. Swift, P. Traykovski, S. Bentley, J. C. Borgeld, C. W. Reed, and A. W. Niedoroda (2004), River flooding, storm resuspension, and event stratigraphy on the northern California shelf: observations compared with simulations, *Mar. Geol.*, *210*(1), 17–41.

Ferry, J., and S. Balachandar (2001), A fast Eulerian method for disperse two-phase flow, *Int. J. Multiphase Flow*, *27*(7), 1199–1226.

Ferry, J., S. L. Rani, and S. Balachandar (2003), A locally implicit improvement of the equilibrium Eulerian method, *Int. J. Multiphase Flow*, *29*(6), 869–891.

Fredsoe, J., and R. Deigaard (1992), *Mechanics of coastal sediment transport. Advanced Series on Ocean Engineering*, vol. 3, World Scientific, Singapore.

Friedrichs, C., and L. Wright (2004), Gravity-driven sediment transport on the continental shelf: implications for equilibrium profiles near river mouths, *Coast. Eng.*, *51*(8-9), 795–811.

Goldsmith, S. T., A. E. Carey, W. B. Lyons, S.-J. Kao, T.-Y. Lee, and J. Chen (2008), Extreme storm events, landscape denudation, and carbon sequestration: Typhoon Mindulle, Choshui River, Taiwan, *Geology*, *36*(6), 483–486.

Hale, R., A. Ogston, J. Walsh, and A. Orpin (2014), Sediment transport and event deposition on the Waipaoa River Shelf, New Zealand, *Cont. Shelf Res.*, *86*(0), 52–65.

Harris, C. K., and P. Wiberg (2002), Across-shelf sediment transport: Interactions between suspended sediment and bed sediment, *J. Geophys. Res.*, *107*(C1), 8–1–8–12.

Harris, C. K., C. K., and P. L. Wiberg (1997), Approaches to quantifying long-term continental shelf sediment transport with an example from the Northern California STRESS mid-shelf site, *Cont. Shelf Res.*, *17*(11), 1389–1418.

Hill, P. S., T. G. Milligan, and W. Geyer (2000), Controls on effective settling velocity of suspended sediment in the Eel River flood plume, *Cont. Shelf Res.*, *20*(16), 2095–2111, Oceanic Flood Sedimentation.

Hsu, T.-J., C. E. Ozdemir, and P. A. Traykovski (2009), High-resolution numerical modeling of wave-supported gravity-driven mudflows, *J. Geophys. Res.*, *114*(C5), C05,014.

Jensen, B., B. Sumer, and J. Fredsoe (1989), Turbulent oscillatory boundary layers at high reynolds numbers, *J. Fluid Mech.*, *206*, 265–297.

Jimenez, J. A., and O. S. Madsen (2003), A simple formula to estimate settling velocity of natural sediments, *J. Waterw. Port, Coast. Ocean Eng.*, *129*(2), 70–78.

Kampf, J., and P. Myrow (2014), High-density mud suspensions and cross-shelf transport: On the mechanism of gelling ignition, *J. Sediment. Res.*, *84*(3), 215–223.

Mehta, A. (1986), Characterization of cohesive sediment properties and transport processes in estuaries, in *Lecture Notes on Coastal and Estuarine Studies*, vol. 14, edited by A. Mehta, pp. 290–325, Springer New York.

Ogston, A., D. Cacchione, R. Sternberg, and G. Kineke (2000), Observations of storm and river flood-driven sediment transport on the northern California continental shelf, *Cont. Shelf Res.*, *20*(16), 2141–2162.

Ozdemir, C. E., T.-J. Hsu, and S. Balachandar (2010), A numerical investigation of fine particle laden flow in an oscillatory channel: the role of particle-induced density stratification, *J. Fluid Mech.*, *665*, 1–45.

Ozdemir, C. E., T.-J. Hsu, and S. Balachandar (2011), A numerical investigation of lutocline dynamics and saturation of fine sediment in the oscillatory boundary layer, *J. Geophys. Res.*, *116*(C9).

Ozdemir, C. E., T.-J. Hsu, and S. Balachandar (2014), Direct numerical simulations of transition and turbulence in smooth-walled stokes boundary layer, *Phys. Fluids*, *26*(4), 045108.

Richardson, J., and W. Zaki (1954), Sedimentation and fluidisation: Part i, *Trans. Instn Chem. Engrs*, *32*(0).

Sanford, L. P., and J. P.-Y. Maa (2001), A unified erosion formulation for fine sediments, *Mar. Geol.*, *179*(1), 9–23.

Traykovski, P., W. Geyer, J. Irish, and J. Lynch (2000), The role of wave-induced density-driven fluid mud flows for cross-shelf transport on the Eel river continental shelf, *Cont. Shelf Res.*, *20*(16), 2113–2140, Oceanic Flood Sedimentation.

Traykovski, P., P. Wiberg, and W. Geyer (2007), Observations and modeling of wave-supported sediment gravity flows on the Po prodelta and comparison to prior observations from the Eel shelf, *Cont. Shelf Res.*, *27*(3-4), 375–399.

Wheatcroft, R., and J. Borgeld (2000), Oceanic flood deposits on the northern California shelf: large-scale distribution and small-scale physical properties, *Cont. Shelf Res.*, *20*(16), 2163–2190.

Wiberg, P. L., D. E. Drake, and D. A. Cacchione (1994), Sediment resuspension and bed armoring during high bottom stress events on the northern California inner continental shelf: measurements and predictions, *Cont. Shelf Res.*, *14*(1011), 1191–1219.

Winterwerp, J. C. (2006), Stratification effects by fine suspended sediment at low, medium, and very high concentrations, *J. Geophys. Res.*, *111*(C5), C05,012.

Winterwerp, J. C. (2007), On the sedimentation rate of cohesive sediment, in *Estuarine and Coastal Fine Sediments Dynamics Intercoh 2003*, vol. Volume 8, edited by L. S. J.P.Y. Maa and D. Schoellhamer, pp. 209–226, Elsevier.

Winterwerp, J. C., and W. G. Van Kesteren (2004), *Introduction to the physics of cohesive sediment dynamics in the marine environment*, Elsevier.

Wright, L., and C. Friedrichs (2006), Gravity-driven sediment transport on continental shelves: A status report, *Cont. Shelf Res.*, *26*(17), 2092–2107.

Yu, X., T.-J. Hsu, and S. Balachandar (2013), A spectral-like turbulence-resolving scheme for fine sediment transport in the bottom boundary layer, *Comput. Geosci.*, *61*(0), 11–22.

Yu, X., C. Ozdemir, T. Hsu, and S. Balachandar (2014), Numerical investigation of turbulence modulation by sediment-induced stratification and enhanced viscosity in oscillatory flows, *J. Waterw. Port, Coast. Ocean Eng.*, *140*(2), 160–172.

Zhou, J., R. J. Adrian, S. Balachandar, and T. M. Kendall (1999), Mechanisms for generating coherent packets of hairpin vortices in channel flow, *J. Fluid Mech.*, *387*, 353–396.